



# Phytic acid-derivative Co<sub>2</sub>B-CoPO<sub>x</sub> coralloidal structure with delicate boron vacancy for enhanced hydrogen generation from sodium borohydride

Luyan Shi<sup>a</sup>, Ke Zhu<sup>a</sup>, Yuting Yang<sup>a</sup>, Qinrui Liang<sup>a</sup>, Qimin Peng<sup>a</sup>, Shuqing Zhou<sup>a</sup>,  
Tayirjan Taylor Isimjan<sup>b,\*</sup>, Xiulin Yang<sup>a,\*</sup>

<sup>a</sup>Guangxi Key Laboratory of Low Carbon Energy Materials, School of Chemistry and Pharmaceutical Sciences, Guangxi Normal University, Guilin 541004, China

<sup>b</sup>Saudi Arabia Basic Industries Corporation (SABIC) at King Abdullah University of Science and Technology (KAUST), Thuwal 23955-6900, Saudi Arabia



## ARTICLE INFO

### Article history:

Received 12 August 2023

Revised 14 October 2023

Accepted 18 October 2023

Available online 22 October 2023

### Keywords:

Co<sub>2</sub>B-CoPO<sub>x</sub> catalyst

P doping

Boron vacancy

NaBH<sub>4</sub> hydrolysis

Hydrogen generation

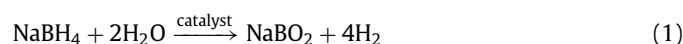
## ABSTRACT

Application of transition metal boride (TMB) catalysts towards hydrolysis of NaBH<sub>4</sub> holds great significance to help relieve the energy crisis. Herein, we present a facile and versatile metal-organic framework (MOF) assisted strategy to prepare Co<sub>2</sub>B-CoPO<sub>x</sub> with massive boron vacancies by introducing phytic acid (PA) cross-linked Co complexes that are acquired from reaction of PA and ZIF-67 into cobalt boride. The PA etching effectively breaks down the structure of ZIF-67 to create more vacancies, favoring the maximal exposure of active sites and elevation of catalytic activity. Experimental results demonstrate a drastic electronic interaction between Co and the dopant phosphorous (P), thereby the robustly electronegative P induces electron redistribution around the metal species, which facilitates the dissociation of B-H bond and the adsorption of H<sub>2</sub>O molecules. The vacancy-rich Co<sub>2</sub>B-CoPO<sub>x</sub> catalyst exhibits scalable performance, characterized by a high hydrogen generation rate (HGR) of 7716.7 mL min<sup>-1</sup> g<sup>-1</sup> and a low activation energy (E<sub>a</sub>) of 44.9 kJ/mol, rivaling state-of-the-art catalysts. This work provides valuable insights for the development of advanced catalysts through P doping and boron vacancy engineering and the design of efficient and sustainable energy conversion systems.

© 2024 Published by Elsevier B.V. on behalf of Chinese Chemical Society and Institute of Materia Medica, Chinese Academy of Medical Sciences.

Hydrogen-related energy devices, including hydrogen-oxygen fuel cells, large-scale hydrogen power generation, and other hydrogen-powered devices, have incentivized the revolution of various hydrogen evolution technologies [1]. In particular, hydrogen storage materials catalytic hydrogen (H<sub>2</sub>) generation technology has been deemed an up-and-coming trend to realize a sustainable energy scheme [2]. Among the chemical storage sources of hydrogen, metal hydrides such as NaBH<sub>4</sub>, LiAlH<sub>4</sub> and MgH<sub>2</sub> have garnered tremendous recent attention [3–5]. Among them, NaBH<sub>4</sub> is emerging as a central focus with a theoretical gravimetric hydrogen storage capacity of 10.6 wt%, excellent hydrolysis controllability, milder operation conditions, and high hydrogen purity, which can be applied to hydrogen production by hydrolysis [6,7]. Moreover, NaBH<sub>4</sub> can facily regenerate from its hydrolytic product, making it possible for the NaBH<sub>4</sub>-H<sub>2</sub>-PEMFC system to be a primary source device for on-demand power supply [8,9]. These ad-

vantages yield NaBH<sub>4</sub> hydrolysis hydrogen production a bright future in real-world applications. Nevertheless, several hurdles need to be addressed before its commercial deployment, including the sluggish kinetic of NaBH<sub>4</sub> self-hydrolysis and low H<sub>2</sub> yield [10]. Exploring efficient catalysts is a feasible strategy for overcoming kinetic barriers for the hydrolysis of NaBH<sub>4</sub>. The ideal hydrolysis reaction of NaBH<sub>4</sub> in the presence of a catalyst is given as Eq. 1 [11]:



However, considerable market barriers still exist because the noble metals (e.g., Ru, Pt, Pd) are the most widely applied catalysts to negotiate the hydrolysis of NaBH<sub>4</sub>, resulting in poor cost competitiveness [12,13]. Alternatively, recent progress in the search of new catalysts has proven that a range of Co-based borides and phosphides are attractive alternatives. Especially, the active sites of Co-based borides have been well identified, which can stimulate the strategy to tailor Co-based borides for promoted NaBH<sub>4</sub> hydrolysis by modulating material parameters such as vacancies and the electronic interaction between transition metal atoms and boron

\* Corresponding authors.

E-mail addresses: [isimjant@sabic.com](mailto:isimjant@sabic.com) (T.T. Isimjan), [xlyang@gxnu.edu.cn](mailto:xlyang@gxnu.edu.cn) (X. Yang).

atoms [14,15]. In addition, high electronegative heteroatom doping can increase the number and modulate the electronic surrounding of metal active sites, thus improving the activities of the catalyst [16]. For example, Mehdi *et al.* reported P-induced Co-based monolithic efficient catalysts for  $\text{NH}_3\text{BH}_3$  hydrolysis and showed that the induction of P caused electron transfer from Co to P, promoting new active sites for the efficient adsorption of reactant molecules [17]. Notably, the highly electronegative phosphorus (P) atom possesses lone-pair electrons in 3p orbitals and vacant 3d orbitals, which can mediate local charge density and change the surface charge state, further advancing the catalytic performance [18]. We assume that the P-induced approach also has a positive effect on the catalyst of  $\text{NaBH}_4$  hydrolysis. However, conventional procedures (gas-solid reaction scheme) use  $\text{NaH}_2\text{PO}_2$  as the P source, which would release poisonous and auto-ignition  $\text{PH}_3$  products into the environment [19]. Phytic acid (PA, myo-inositol 1,2,3,4,5,6-hexakisphosphate) is a naturally environmentally friendly and renewable biological compound, and its six phosphate groups can easily chelate to different metal ions, which can serve as an ideal P source to replace  $\text{NaH}_2\text{PO}_2$  [20]. In the processes of PA etching, P possesses higher electronegativity than metallic (M) atoms, which tend to receive electrons from the metal, causing a redistribution of the electronic properties of the catalysts and further forming the key active sites favoring the interaction and adsorption with reaction intermediates [21]. On the other hand, vacancy engineering is considered a new "intrinsic" strategy to enhance catalytic activity by inducing high distortion energy and diverse atomic rearrangements [22]. Besides, vacancies can manipulate the electronic band structure as well as lower the activation energy of adsorption and dissociation of reactants [23]. Consequently, the electronic structure and surface nature of the catalyst are two versatile knobs for enhancing the intrinsic catalytic activity, which can be favorably tailored through doping and vacancy engineering.

In this work, a light P doping and rich boron vacancies  $\text{Co}_2\text{B-CoPO}_x$  was developed as a highly efficient catalyst for  $\text{NaBH}_4$  hydrolysis. The coraloidal structure of  $\text{Co}_2\text{B-CoPO}_x$  is porous with an average pore size of about 23.8 nm. Such unique structural features not only provide more active sites but also may improve electron transfer dynamics, beneficial to the hydrolysis of  $\text{NaBH}_4$ . Moreover, the experimental and characteristic analyses show that the doping of P tunes the relative content of B and induces more boron vacancies, which subsequently affects the electronic structure and facilitates the reversible dissociation of B-H on active sites. As a result,  $\text{Co}_2\text{B-CoPO}_x$  exhibits excellent hydrolysis activity and scalable reusability. Importantly, the prepared robust  $\text{Co}_2\text{B-CoPO}_x$  catalyst reveals remarkably efficient hydrogen evolution from  $\text{NaBH}_4$  in comparison to previous non-noble catalysts and even noble catalysts presented in the literature. Our work provides new opportunities for designing advanced metal borides catalysts for the hydrolysis of  $\text{NaBH}_4$  toward improved viability in generating  $\text{H}_2$  from  $\text{NaBH}_4$ .

The synthesis procedure of  $\text{Co}_2\text{B-CoPO}_x$  is elaborated in Fig. 1a. Initially, uniform Co-based zeolitic imidazolate framework-67 (ZIF-67) nanocubes (NCs) were synthesized using a surfactant-assisted approach. The successful synthesis of ZIF-67 NCs was confirmed by the X-ray diffraction (XRD) pattern in Fig. S1 (Supporting information), which matched well with the simulated ZIF-67 [24]. Forming the chelation structure of P-O-Co in the precursor is notoriously challenging that requires pertinent chelation structure engineering. We present a PA-assisted method to achieve such goal, where PA coordinated with  $\text{Co}^{2+}$  through its six negatively charged phosphate groups to form Co-PA. During this process, PA acted as an organic acid to release proton, breaking the chelation of  $\text{Co}^{2+}$  and 2-methylimidazole, resulting in the loss of a portion of the organic ligands in ZIF-67. Simultaneously, PA also coordinated with  $\text{Co}^{2+}$  through P-O-M and served as a P source. The chemical etch-

ing and coordination reaction in the PA solution transformed ZIF-67 into amorphous Co-PA, as observed from the disappearance of ZIF-67 peaks and the formation of amorphous Co-PA in Fig. S1. Next, Co-PA was ground with  $\text{CoCl}_2 \cdot 6\text{H}_2\text{O}$  and urea, followed by boronation using  $\text{NaBH}_4$ , to convert it into  $\text{Co}_2\text{B-CoPO}_x$ . The XRD pattern of  $\text{Co}_2\text{B-CoPO}_x$  in Fig. 1b confirmed that all the diffraction peaks can be indexed well to  $\text{Co}_2\text{B}$  (JCPDS No. 25-0241). The weak and broad diffraction peaks indicated that the  $\text{Co}_2\text{B}$  crystallites were in the nanometer size range, and the crystallinity was weak [25]. Control samples were also characterized using XRD. Fig. S2a (Supporting information) showed that the diffraction pattern of  $\text{Co}_2\text{B-ZIF-67}$  was similar to that of ZIF-67 but slightly protruded at  $30^\circ$ – $40^\circ$  and  $40^\circ$ – $50^\circ$ , indicating the presence of  $\text{Co}_2\text{B}$  in the sample. Fig. S2b (Supporting information) confirmed the formation of the control sample  $\text{Co}_2\text{B}$  (JCPDS No. 25-0241). Figs. S3a and b (Supporting information) showed that ZIF-67-urea and Co-PA-urea were the amorphous structure.

Fourier transform infrared (FT-IR) measurement was conducted to probe the local binding structure of Co during the reaction process (Fig. S4 in Supporting information). The peaks observed around  $423\text{ cm}^{-1}$  correspond to the Co-N bonding of 2-methylimidazole, while the peaks around  $2900\text{ cm}^{-1}$  are associated with the C-H stretching vibration of the methyl group [26]. After the chemical etching in PA solution, the intensity of these peaks diminished in both Co-PA and  $\text{Co}_2\text{B-CoPO}_x$ , revealing the substitution of 2-methylimidazole by PA and the formation of PA cross-linked Co complexes [27]. The  $\text{N}_2$  absorption/desorption isotherms of  $\text{Co}_2\text{B-CoPO}_x$  and  $\text{Co}_2\text{B-ZIF-67}$  are shown in Fig. S5 (Supporting information), exhibiting a typical type IV isotherm, suggesting the presence of mesopores. The Brunauer-Emmett-Teller (BET) surface area of  $\text{Co}_2\text{B-CoPO}_x$  was calculated to be  $15.5\text{ m}^2/\text{g}$ , which is lower than that of  $\text{Co}_2\text{B-ZIF-67}$  ( $736.3\text{ m}^2/\text{g}$ ). The decreased BET specific surface area can be ascribed to the partially disrupted structure of ZIF-67 in phytic acid solution. The reduction in surface area further supports the coordination of  $\text{Co}^{2+}$  with PA, which predicts improved electronic structure [28,29]. Additionally, the pore size distribution of  $\text{Co}_2\text{B-CoPO}_x$  is 23.8 nm, significantly larger than that of  $\text{Co}_2\text{B-ZIF-67}$  (2.6 nm), which well endows  $\text{Co}_2\text{B-CoPO}_x$  with higher catalytic activity by providing more active sites and helping the  $\text{H}_2$  to diffuse along the surface (the inset of Fig. S5) [30]. Electron paramagnetic resonance (EPR) has been proved to be an effective tool to characterize the vacancies in the catalysts. As depicted in Fig. 1c, a distinct signal around  $g=2.006$  was observed, which can be assigned to the unpaired electrons trapped by boron vacancies [31]. A monotonic increase in the boron vacancy concentration is observed with increasing volume of PA. It should be noted that the B content decreased from 11.9 wt% for  $\text{Co}_2\text{B-ZIF-67}$  to 9.2 wt% for  $\text{Co}_2\text{B-CoPO}_x$ , as confirmed by inductively coupled plasma mass spectroscopy (ICP-MS) measurements (Table S1 in Supporting information). This suggests that phosphorization after PA treatment resulted in a slight loss of B atoms and the creation of more boron vacancies [32,33]. Additionally, the introduction of P species into ZIF-67 lead to a different bonding environment for Co-O-P bonds compared to original N-Co-N structure, which contributed to the disorder of lattice cell and the formation of more boron vacancies [34]. The increased number of boron vacancies in  $\text{Co}_2\text{B-CoPO}_x$  substantially modify its electronic structure and provided active sites for  $\text{NaBH}_4$  adsorption, leading to enhanced catalytic activity [35].

The morphological evolution of  $\text{Co}_2\text{B-CoPO}_x$  composite was tracked using scanning electron microscope (SEM). Fig. S6a (Supporting information) shows that the initially formed purple ZIF-67 consists exclusively of uniform nanocubes. After PA etching, the SEM image reveals that the obtained pink Co-PA exhibits a nanoparticles morphology with rough edges, and the nanoparticles are in contact with each other (Fig. S6b in Supporting information).

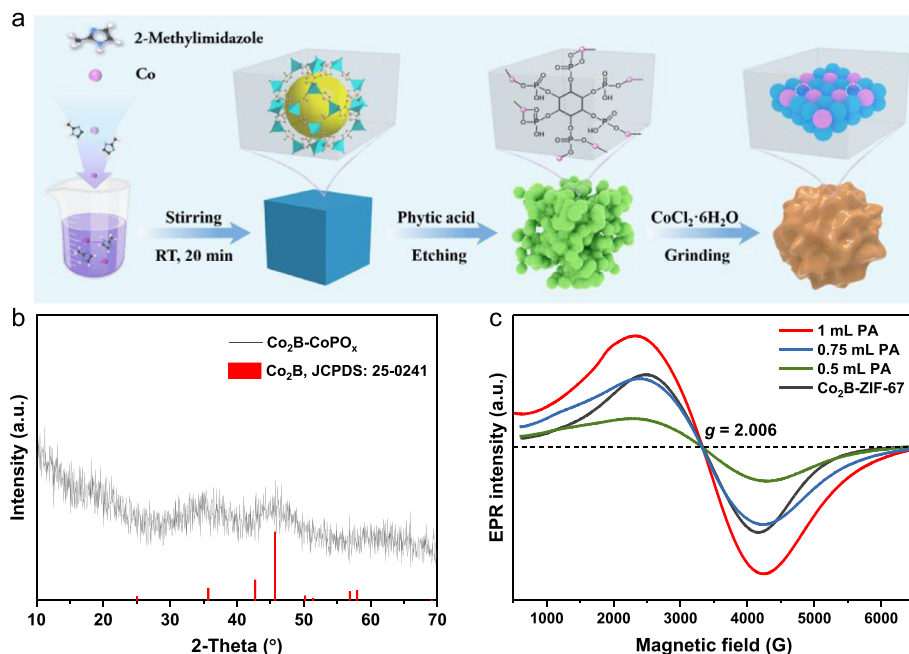


Fig. 1. (a) Schematic diagram for the preparation of  $\text{Co}_2\text{B-CoPO}_x$ . (b) XRD pattern of  $\text{Co}_2\text{B-CoPO}_x$ . (c) EPR spectra of as-synthesized samples at different volume of PA.

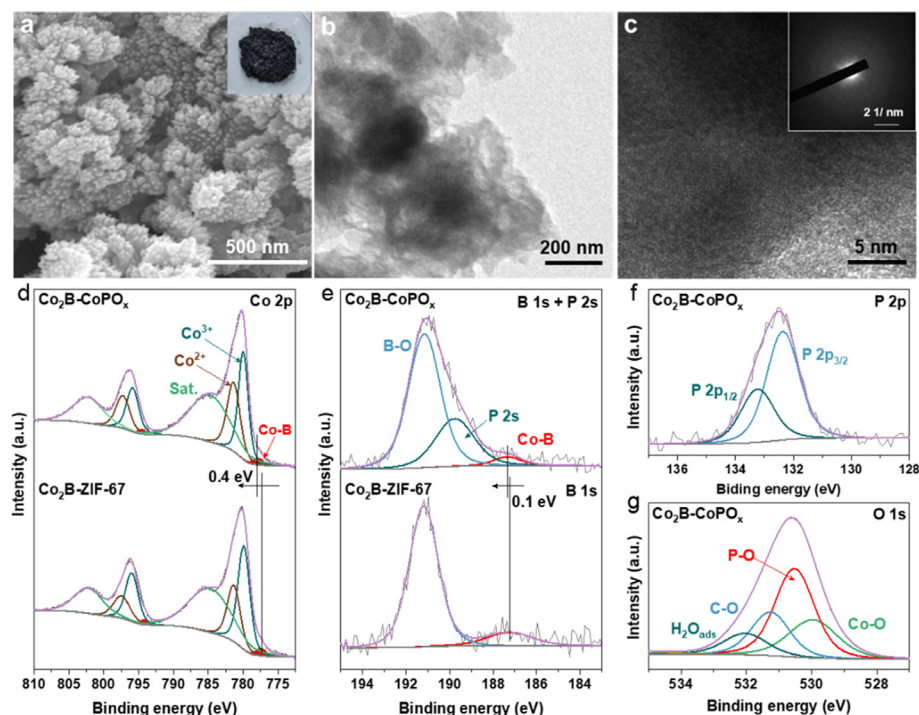
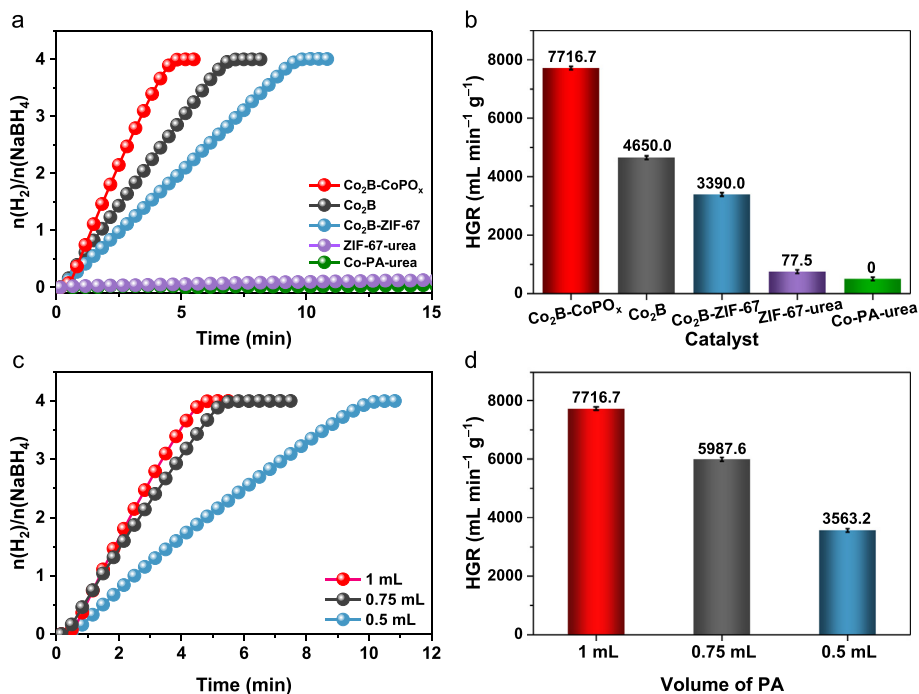


Fig. 2. (a) SEM image of  $\text{Co}_2\text{B-CoPO}_x$ . (b) TEM and (c) high-resolution TEM (HR-TEM) images of  $\text{Co}_2\text{B-CoPO}_x$  (inset: SADE pattern). High resolution XPS spectra of (d) Co 2p and (e) B 1s for  $\text{Co}_2\text{B-CoPO}_x$  and  $\text{Co}_2\text{B-ZIF-67}$ . (f) P 2p and (g) O 1s for  $\text{Co}_2\text{B-CoPO}_x$ .

These significant morphological changes are related to the dissolution of organic ligands, which causes the disintegration and reorganization of the nanocubes structure. As the boronizing process proceeds, a well-developed, defined coral-like three-dimensional (3D) morphology of  $\text{Co}_2\text{B-CoPO}_x$  is formed (Fig. 2a). This coral-like infrastructure favors the close contact of reactants with active sites and promotes  $\text{H}_2$  diffusion [36]. In contrast,  $\text{Co}_2\text{B-ZIF-67}$  still inherits the cubic morphology (Fig. S7 in Supporting information), indicating the crucial role of PA in the formation of the coral-like structure of  $\text{Co}_2\text{B-CoPO}_x$ . The microstructure of  $\text{Co}_2\text{B-}$

$\text{CoPO}_x$  is further examined by transmission electron microscopy (TEM). The low-magnification TEM image shows that  $\text{Co}_2\text{B-CoPO}_x$  presents a porous structure (Fig. 2b). Moreover, the high-resolution TEM (HR-TEM) image reveals the absence of well-resolved lattice fringes (Fig. 2c). The corresponding selected area electron diffraction (SADE) pattern exhibits halo rings (Fig. 2c, inset), verifying the formation of a weak crystalline structure that is consistent with the XRD results. The energy dispersive X-ray (EDX) pattern proves the co-existence of Co, B, P, and O elements (Fig. S6c in Supporting information). The high-angle annular dark-field scanning TEM



**Fig. 3.** (a) The equivalent H<sub>2</sub> per mole of sodium borohydride versus time with different catalysts and (b) the corresponding HGR values. (c) The equivalent H<sub>2</sub> per mole of sodium borohydride versus time with different volume of PA and (d) the corresponding HGR values.

(HAADF-STEM) and EDX mapping images demonstrate the homogeneous distribution of Co, B, P, and O elements (Fig. S6d in Supporting information).

The practical structure and elemental chemical state of Co<sub>2</sub>B-CoPO<sub>x</sub> were elucidated by X-ray photoelectron spectroscopy (XPS). The XPS survey spectrum of Co<sub>2</sub>B-CoPO<sub>x</sub> corroborated the presence of Co, B, P and O elements (Fig. S8a in Supporting information), while only Co, B and O were observed in Co<sub>2</sub>B-ZIF-67, manifesting the successful doping of P. The high-resolution C 1s spectra were deconvoluted into four peaks corresponding to C=C (284.0 eV), C-C (284.8 eV), C-O (286.0 eV) and C=O (288.5 eV) (Figs. S8b and c in Supporting information), which served as a calibration standard [37]. The Co 2p XPS spectrum exhibited two blunt satellite peaks and two sharp peaks, corresponding to the spin-orbit splitting of the Co 2p<sub>3/2</sub> and 2p<sub>1/2</sub> components, respectively (Fig. 2d) [38]. The two prominent peaks at 779.9 eV and 781.3 eV were assigned to Co<sup>3+</sup> and Co<sup>2+</sup> in the Co 2p<sub>3/2</sub> region [39,40]. Simultaneously, the other two fitted peaks at around 777.8 and 784.7 eV were attributed to Co-B bonding and shake-up satellites, respectively [41]. The coexistence of Co<sup>3+</sup> and Co<sup>2+</sup> suggests a fraction of Co<sup>3+</sup> is reduced to Co<sup>2+</sup> by excessive NaBH<sub>4</sub> to form B vacancies [42]. In Fig. 2e, the characteristic peaks at 187.2 and 191.2 eV corresponded to Co-B and B-O bonding in Co<sub>2</sub>B-ZIF-67 [43]. In Co<sub>2</sub>B-CoPO<sub>x</sub>, a slight positive shift of Co-B bond was observed, and the appearance of the P 2s peak indicated the presence of phosphate. The positive shift demonstrates a drastic electronic coupling between Co-B and phosphate, where phosphate has strong electronegativity and can draw electrons from Co-B species [44,45]. The P 2p high-resolution XPS spectrum of Co<sub>2</sub>B-CoPO<sub>x</sub> was disassembled into two sets of peaks corresponding to P 2p<sub>3/2</sub> and P 2p<sub>1/2</sub> (Fig. 2f), further validating the successful induction of phosphate in the Co<sub>2</sub>B-CoPO<sub>x</sub> catalyst [46]. The O 1s spectra of Co<sub>2</sub>B-CoPO<sub>x</sub> (Fig. 2g) showed peaks at approximately 529.9, 530.5, 531.3, and 532.0 eV, which can be considered as Co-O, P-O, C-O and H<sub>2</sub>O<sub>ads</sub>, respectively [47,48]. As depicted in Fig. S9 (Supporting information) Co<sub>2</sub>B-CoPO<sub>x</sub> (19.3) has a smaller contact angle compared to Co<sub>2</sub>B-ZIF-67 (51.2), elucidating that Co<sub>2</sub>B-CoPO<sub>x</sub> possesses

higher hydrophilicity. The presence of a mass of hydroxyl groups enhances the contact between the NaBH<sub>4</sub> solution and the catalyst, thereby improving the catalytic performance [49]. Overall, the introduction of phosphate species and B vacancies effectively regulates the electronic structure and local coordination environment of Co centers, thereby accelerating electron transport and boosting the hydrolysis of NaBH<sub>4</sub> [50]. Consequently, Co<sub>2</sub>B-CoPO<sub>x</sub> possesses superior catalytic activity compared to Co<sub>2</sub>B-ZIF-67, with catalysis results discussed below later [51].

The catalytic activities were assessed in an alkaline NaBH<sub>4</sub> solution at 25 °C using a water displacement method, as illustrated in Fig. S10 (Supporting information). To investigate the role of P doping in improving NaBH<sub>4</sub> hydrolysis for H<sub>2</sub> production, we carried out control experiments using weak acid without P (oxalic acid) for etching the catalysts and investigated the difference in performance. As shown in Figs. S11a and b (Supporting information), catalysts etched with the same pH of oxalic acid exhibited poor hydrolysis activity, with an HGR value of 1881.5 mL min<sup>-1</sup> g<sup>-1</sup>. This is in sharp contrast to the Co<sub>2</sub>B-CoPO<sub>x</sub> etched with PA, which displayed significant catalytic activity with an HGR value of 7716.7 mL min<sup>-1</sup> g<sup>-1</sup>. This fully confirms that P is a crucial factor in determining the catalyst's high activity. In addition, somewhat delayed hydrogen evolution was observed for all samples, due to initial catalyst wetting and pore diffusion resistance [52].

As exhibited in Figs. 3a and b, directly grinding ZIF-67 and Co-PA resulted in impaired activity, suggesting that effective active sites of Co<sub>2</sub>B cannot be formed through this method. However, after PA treatment and the second step of boronation, Co<sub>2</sub>B-CoPO<sub>x</sub> exhibited remarkably enhanced catalytic activity, completing the hydrolysis of NaBH<sub>4</sub> in only 4.8 min with an HGR value of 7716.7 mL min<sup>-1</sup> g<sup>-1</sup>. In comparison, Co<sub>2</sub>B-ZIF-67 and Co<sub>2</sub>B showed inferior activity, requiring 9.7 min (HGR = 3390.0 mL min<sup>-1</sup> g<sup>-1</sup>) and 7.0 min (HGR = 3390.0 mL min<sup>-1</sup> g<sup>-1</sup>), respectively, to complete the full reaction. This highlights the critical impact of P doping and B vacancy engineering on the catalytic property of the material. To optimize the proportion of PA, different volumes (0.5, 0.75, 1, 1.25 and 1.5 mL) of PA were introduced into

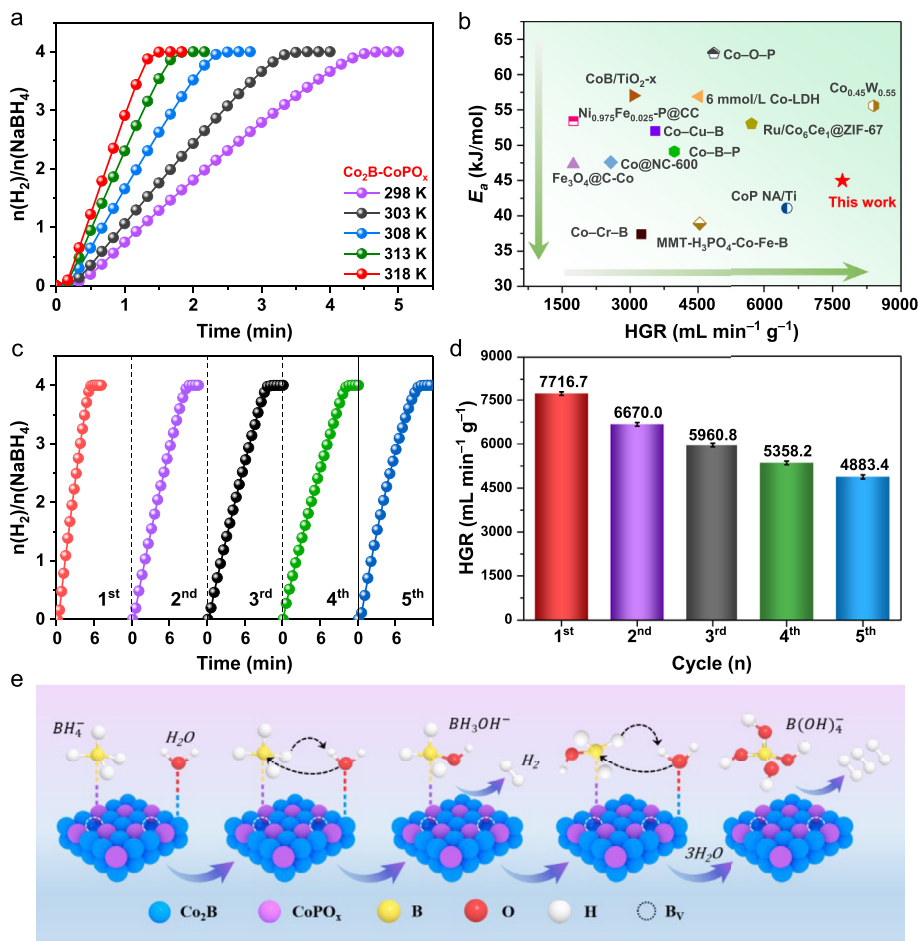


**Fig. 4.** (a) Curves of hydrolysis of alkaline NaBH<sub>4</sub> solution with different reaction temperatures in the range of 298–318 K. (b) Comparison of the HGR and  $E_a$  values of Co<sub>2</sub>B-CoPO<sub>x</sub> with other recently reported catalysts. (c) Reusability test of Co<sub>2</sub>B-CoPO<sub>x</sub> catalyst in alkaline NaBH<sub>4</sub> solution at 25 °C and (d) the corresponding HGR values in the different cycle. (e) The proposed mechanism diagram of NaBH<sub>4</sub> hydrolysis for H<sub>2</sub> generation.

the ethanol solution. Figs. 3c and d show that 1 mL of PA possessed the most remarkable hydrogen generation rate, while 1.25 mL and 1.5 mL of PA exhibited inactive behavior. The above phenomenon can be attributed to the following reasons: when the volume of PA is 0.5 and 0.75 mL, the solution appears purple and light pink-purple, respectively, indicating insufficient etching of ZIF-67 by PA and leading to a small HGR value (Fig. S12 in Supporting information). On the other hand, as the volume of PA increases from 1.25 to 1.5 mL, the solution turns brown or even transparent, demonstrating the complete dissolution of ZIF-67 due to the high concentration of H<sup>+</sup> induced by a large amount of PA. The surface vacancies of catalysts may induce positive effects on the hydrogen generation of NaBH<sub>4</sub>. We next tried to quantify the boron vacancies by XPS to unveil the vacancy-activity relationship. The content ratio was calculated based on the proportion of its fitting peaks [53]. The EPR spectra demonstrated the concentration of boron vacancies can be modulated by phosphorus doping content [54]. The content ratio of P is 29.0%, 21.1% and 17.2% for Co<sub>2</sub>B-CoPO<sub>x</sub>-1 mL, Co<sub>2</sub>B-CoPO<sub>x</sub>-0.75 mL and Co<sub>2</sub>B-CoPO<sub>x</sub>-0.5 mL, respectively (Fig. S13 in Supporting information). It can be seen the general increase in boron vacancies concentration with the increase of PA. Then, we investigated the effect of boron content on hydrolysis of NaBH<sub>4</sub>. Fig. 3d showed that the HGR value was apparent increase when the volume of PA was increased from 0.5 mL to 1 mL. Hence, more boron vacancies can contribute the hydrolysis of NaBH<sub>4</sub>.

NaOH is usually introduced as a stabilizer into the NaBH<sub>4</sub> hydrolysis system to prevent self-hydrolysis. In the absence of a cata-

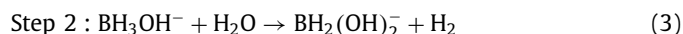
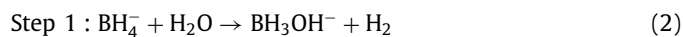
lyst, self-hydrolysis of 150 mmol/L NaBH<sub>4</sub> solution takes about 10 h to produce 110 mL of H<sub>2</sub> and negligible hydrogen gas is produced from 150 mmol/L NaBH<sub>4</sub> + 0.4 wt% NaOH solution, verifying the stability of NaBH<sub>4</sub> in water and an alkaline environment (Fig. S14 in Supporting information). To further explore the effect of NaOH, hydrogen production with different concentrations of NaOH was carried out under the same conditions. Fig. S15a (Supporting information) shows that the addition of NaOH significantly promotes the catalytic hydrolysis of NaBH<sub>4</sub>, and the H<sub>2</sub> generation rate barely changed as NaOH concentrations increased from 0.4 wt% to 3 wt%. However, a further increase of NaOH concentration (from 3 wt% to 10 wt%) leads to a decrease in HGR. As reported by others, the hydrolysis mechanism of NaBH<sub>4</sub> differs on utilization of different catalysts [55,56]. In this work, the OH<sup>-</sup> ions play a dual role during the catalytic hydrolysis reaction. Appropriate concentration of OH<sup>-</sup> ions can activate active sites, thereby enhancing catalytic activity. The higher NaOH concentration results in the increase in viscosity and the alkalinity of the solution, inhibiting the hydrolysis reaction [57]. Therefore, 0.4 wt% NaOH was selected as the optimal concentration to avoid reagent waste. The influence of NaBH<sub>4</sub> concentrations on the hydrolysis catalyzed by Co<sub>2</sub>B-CoPO<sub>x</sub> was also investigated (Fig. S15b in Supporting information). The H<sub>2</sub> generation rate versus the concentration of NaBH<sub>4</sub> is plotted on a natural logarithmic scale in the inset of Fig. S15b. The slope of the logarithmic plot is 0.083, indicating a zero-order reaction with respect to NaBH<sub>4</sub> concentration [58]. This unveils that NaBH<sub>4</sub> is easily activated, and its activation is not the rate-determining step in the

hydrolysis process [59]. The amount of catalyst is another decisive factor in determining the catalytic reaction rate. As seen in Figs. S15c and d (Supporting information), the hydrogen generation rate of Co<sub>2</sub>B-CoPO<sub>x</sub> varied with the change in catalyst mass from 5 mg to 20 mg. Among the series, 10 mg of Co<sub>2</sub>B-CoPO<sub>x</sub> exhibited the highest hydrogen generation rate, making it the optimal amount of catalyst and resulting in substantial cost reduction.

The effect of P doping on the activation energy in NaBH<sub>4</sub> hydrolysis was explored by investigating the temperature dependence of hydrogen generation kinetics at different temperatures, as shown in Fig. 4a and Fig. S16a (Supporting information). Based on the Arrhenius plots, the activation energy (*E<sub>a</sub>*) value of Co<sub>2</sub>B-CoPO<sub>x</sub> was calculated to be 44.9 kJ/mol, which is lower than that of Co<sub>2</sub>B-ZIF-67 (56.1 kJ/mol) (Fig. S16b in Supporting information), and significantly lower than the values reported for most non-noble or noble metal catalysts in previous literature (Fig. 4b). This validates that P doping effectively reduced the energy barrier for molecule activation. Hydrogen generation with NH<sub>3</sub>BH<sub>3</sub> is proceeded under a similar method. A HGR of 1891.9 mL min<sup>-1</sup> g<sup>-1</sup> is achieved (Fig. S17 in Supporting information). Compared with NaBH<sub>4</sub> (7716.7 mL min<sup>-1</sup> g<sup>-1</sup>), a decreased activity is emerged for NH<sub>3</sub>BH<sub>3</sub> hydrolysis. This negative activity is attributed to the discrepant catalytic mechanism during borohydride hydrolysis caused by the different molecular geometry of NaBH<sub>4</sub> and NH<sub>3</sub>BH<sub>3</sub> [60]. The reusability is very important for catalysts in the aspect of the practical application. Therefore, the reusability of Co<sub>2</sub>B-CoPO<sub>x</sub> catalyst was evaluated through a continuous recycling test of catalytic NaBH<sub>4</sub> hydrolysis. As depicted in Figs. 4c and d, the catalyst exhibited a slight degradation in activity after 5 cycles. As demonstrated in Fig. S18 (Supporting information), the XRD pattern shows that the Co<sub>2</sub>B-CoPO<sub>x</sub> after 5 cycles keeps a similar structural composition. Moreover, XPS analysis (Fig. S19 in Supporting information) exhibits that the original elemental composition, chemical state and the peak intensities were similar to Co<sub>2</sub>B-CoPO<sub>x</sub> even after 5 cycles. These results clearly indicate that our developed catalyst bears a stable coralloidal structure. The SEM images show that the catalyst's surface occurs agglomerations after catalyzing the hydrolysis of NaBH<sub>4</sub> (Fig. S20 in Supporting information). Therefore, the slight decrease in catalytic activity can be attributed to surface agglomeration and accumulation of metaborate on the catalyst surface, resulting in a reduction of boron vacancies and thus hindering electron transmission [61,62]. Overall, the Co<sub>2</sub>B-CoPO<sub>x</sub> catalyst demonstrated outstanding activity and reusability, making it cost-effective and suitable for practical industrial applications.

We next tried to shed light on the underlying origin of the striking catalysis performance of Co<sub>2</sub>B-CoPO<sub>x</sub> based on Langmuir-Hinshelwood model and many previous literatures, the plausible mechanism for NaBH<sub>4</sub> hydrolysis over Co<sub>2</sub>B-CoPO<sub>x</sub> catalyst is shown in Eqs. 2–5 and Fig. 4e [55,61,63]. According to XPS study, P species, being strongly electronegative, draw electrons from Co<sub>2</sub>B, resulting in a higher electron density on CoPO<sub>x</sub> species compared to Co<sub>2</sub>B species. Consequently, the B atoms with a few positive charges in BH<sub>4</sub><sup>-</sup> ions are adsorbed by the electron-rich CoPO<sub>x</sub> species through the binding sites provided by boron vacancies, while the electron-deficient Co<sub>2</sub>B species adsorb H<sub>2</sub>O molecules. In step 1, the adsorbed water molecule attacks BH<sub>4</sub><sup>-</sup>. Consequently, one molecule of H<sub>2</sub> is released and an adsorbed BH<sub>3</sub>OH<sup>-</sup> is left on the surface. In step 2, another adsorbed H<sub>2</sub>O molecule attacks BH<sub>3</sub>OH<sup>-</sup>, and the second H<sub>2</sub> molecule is released and the BH<sub>2</sub>(OH)<sub>2</sub><sup>-</sup> is produced and left on the CoPO<sub>x</sub> species surface. In step 3, a new H<sub>2</sub>O molecule adsorbs at Co<sub>2</sub>B species and attacks BH<sub>2</sub>(OH)<sub>2</sub><sup>-</sup> to produce BH(OH)<sub>3</sub><sup>-</sup> and H<sub>2</sub>. In step 4, H<sub>2</sub>O molecule attacks BH(OH)<sub>3</sub><sup>-</sup> to give H<sub>2</sub> and B(OH)<sub>4</sub><sup>-</sup>. Meanwhile, the B(OH)<sub>4</sub><sup>-</sup> is desorbed. Therefore, the hydrolysis reaction ends with complete conversion of BH<sub>4</sub><sup>-</sup> ion to B(OH)<sub>4</sub><sup>-</sup> ion with release of four H<sub>2</sub> molecules [64]. This mechanism highlights the role

of P doping and B vacancy engineering in the Co<sub>2</sub>B-CoPO<sub>x</sub> catalyst, where P enhances the electron density of CoPO<sub>x</sub> species, facilitating the adsorption of B atoms through boron vacancies. This unique interaction between the catalyst and reactants promotes the efficient hydrolysis of NaBH<sub>4</sub>, leading to enhanced catalytic activity and hydrogen generation.



In conclusion, we report that the P doping rich boron vacancy on Co<sub>2</sub>B-CoPO<sub>x</sub> can be achieved through chelating Co with negatively charged phosphate groups. The rational P doping strategy simultaneously realized the high-level chemical induction and defects in the catalyst. The presence of abundant boron vacancy enhances the catalyst's capacity to capture and interact with reaction intermediates effectively. The high electronegativity of P species serves as an electronic structure modifier to tune the local charge of Co via electron transfer, creating favorable condition for the dissociation of B-H and O-H bonds and rendering impressive catalytic activity. The hydrolysis of NaBH<sub>4</sub> measurements certify the exceptional activity of Co<sub>2</sub>B-CoPO<sub>x</sub>, with a hydrogen generation rate (HGR) of 7716.7 mL min<sup>-1</sup> g<sup>-1</sup>, which is 2.3 times higher than that of Co<sub>2</sub>B-ZIF-67. Furthermore, Co<sub>2</sub>B-CoPO<sub>x</sub> exhibited superior reusability, making it highly promising for practical large-scale applications. These findings provide important design guidance for various hydrogen-involving applications, offering new opportunities for the development of efficient and sustainable energy systems.

## Declaration of competing interest

The authors declare that they have no known competing financial interests or personal relationships that could have appeared to influence the work reported in this paper.

## Acknowledgments

This work has been supported by the National Natural Science Foundation of China (No. 21965005), Natural Science Foundation of Guangxi Province (No. 2021GXNSFAA076001), Guangxi Technology Base and Talent Subject (Nos. GUIKE AD18126001, GUIKE AD20297039), and Innovation Project of Guangxi Graduate Education (Nos. YCSW2023140, YCBZ2023062).

## Supplementary materials

Supplementary material associated with this article can be found, in the online version, at doi:10.1016/j.ccllet.2023.109222.

## References

- [1] M. Li, Z. Zhao, Z. Xia, et al., *Angew. Chem. Int. Ed.* 60 (2021) 8243–8250.
- [2] Z. Gao, G. Wang, T. Lei, et al., *Nat. Commun.* 13 (2022) 118.
- [3] S.S. Liu, Z.B. Li, C.L. Jiao, et al., *Int. J. Hydrog. Energy* 38 (2013) 2770–2777.
- [4] C. Saka, *Appl. Catal. B: Environ.* 292 (2021) 120165.
- [5] Q. Yao, X. Zhang, Z.H. Lu, Q. Xu, *Coord. Chem. Rev.* 493 (2023) 215302.
- [6] L. Ouyang, W. Chen, J. Liu, et al., *Adv. Energy Mater.* 7 (2017) 1700299.
- [7] L. Yao, X. Li, W. Peng, et al., *Inorg. Chem. Front.* 8 (2021) 1056–1065.
- [8] Y. Zhu, L. Ouyang, H. Zhong, et al., *Angew. Chem. Int. Ed.* 59 (2020) 8623–8629.
- [9] H.X. Nunes, D.L. Silva, C.M. Rangel, A.M.F.R. Pinto, *Energies* 14 (2021) 3567.
- [10] A.F. Baye, M.W. Abebe, R. Appiah-Ntiamoah, H. Kim, *J. Colloid Interface Sci.* 543 (2019) 273–284.

- [11] H. Zhang, G. Xu, L. Zhang, et al., *Renew. Energy* 162 (2020) 345–354.
- [12] X. Zhang, X. Sun, D. Xu, et al., *Appl. Surf. Sci.* 469 (2019) 764–769.
- [13] C. Wu, J. Guo, J. Zhang, et al., *Renew. Energy* 136 (2019) 1064–1070.
- [14] X. Wang, J. Liao, H. Li, H. Wang, R. Wang, *Int. J. Hydrog. Energy* 42 (2017) 6646–6656.
- [15] Z. Liu, Y. Tian, S. Li, et al., *Adv. Funct. Mater.* 33 (2023) 2301994.
- [16] H. Sun, J. Meng, L. Jiao, F. Cheng, J. Chen, *Inorg. Chem. Front.* 5 (2018) 760–772.
- [17] S. Mehdi, Y. Liu, H. Wei, et al., *Appl. Catal. B: Environ.* 325 (2023) 122317.
- [18] Z. Xiao, Y. Wang, Y.C. Huang, et al., *Energy Environ. Sci.* 10 (2017) 2563–2569.
- [19] Y. Fan, Y. Zhou, L. Zhang, Y. Feng, K. Shih, *Sep. Purif. Technol.* 264 (2021) 118367.
- [20] G. Zhang, G. Wang, Y. Liu, et al., *J. Am. Chem. Soc.* 138 (2016) 14686–14693.
- [21] J. Zhang, J. Zhang, F. He, et al., *Nano Micro Lett.* 13 (2021) 65.
- [22] X. Wang, Y. Zhang, H. Si, et al., *J. Am. Chem. Soc.* 142 (2020) 4298–4308.
- [23] W. Zhong, Z. Wang, N. Gao, et al., *Angew. Chem. Int. Ed.* 59 (2020) 22743–22748.
- [24] Y. Shan, M. Zhang, Y. Bai, et al., *Chem. Eng. J.* 429 (2022) 132146.
- [25] L. He, Y. Cheng, Q. Li, et al., *Chem. Eng. J.* 453 (2023) 139566.
- [26] S. Sun, Y. Tang, C. Wu, C. Wan, *Anal. Chim. Acta* 1107 (2020) 55–62.
- [27] X. Wang, Z. Na, D. Yin, et al., *ACS Nano* 12 (2018) 12238–12246.
- [28] T. Chen, F. Wang, S. Cao, et al., *Adv. Mater.* 34 (2022) 2201779.
- [29] W. Peng, S. Liu, X. Li, et al., *Chin. Chem. Lett.* 33 (2022) 1403–1406.
- [30] C. Yan, Q. Ma, F. Wang, et al., *Chem. Eng. J.* 433 (2022) 133651.
- [31] P. Wu, Q. Jia, J. He, et al., *J. Hazard. Mater.* 391 (2020) 122183.
- [32] J. Xiong, J. Luo, L. Yang, et al., *J. Ind. Eng. Chem.* 64 (2018) 383–389.
- [33] D. Chen, Y. Wu, Z. Huang, J. Chen, *Nano Micro Lett.* 14 (2022) 156.
- [34] L. Liu, J. Liu, K. Sun, et al., *Chem. Eng. J.* 411 (2021) 128629.
- [35] D. Roy, K. Panigrahi, B.K. Das, et al., *Nanoscale Adv.* 3 (2021) 4739–4749.
- [36] X. Chen, P. Ye, H. Wang, et al., *Adv. Funct. Mater.* 33 (2023) 2212915.
- [37] Y. Yang, Y. Huang, S. Zhou, et al., *J. Energy Chem.* 72 (2022) 395–404.
- [38] C. Wang, L.L. Gu, S.Y. Qiu, et al., *Appl. Catal. B: Environ.* 297 (2021) 120452.
- [39] K. Zeng, W. Li, Y. Zhou, et al., *Chem. Eng. J.* 421 (2021) 127831.
- [40] K. Xiang, D. Wu, Y. Fan, et al., *Chem. Eng. J.* 425 (2021) 130583.
- [41] X. Qiao, H. Kang, Y. Li, et al., *Appl. Catal. B: Environ.* 305 (2022) 121034.
- [42] M. Asnavandi, Y. Yin, Y. Li, C. Sun, C. Zhao, *ACS Energy Lett.* 3 (2018) 1515–1520.
- [43] K. Zhang, G. Zhang, J. Qu, H. Liu, *Small* 14 (2018) 1802760.
- [44] X. Wang, C. Sun, F. He, et al., *ACS Appl. Mater. Interfaces* 11 (2019) 32460–32468.
- [45] S.J. Sittler, K.S. Raja, I. Charit, *J. Electrochem. Soc.* 163 (2016) H1069–H1075.
- [46] W. Li, Y. Li, H. Fu, et al., *Chem. Eng. J.* 381 (2020) 122683.
- [47] M. Zhang, Y. Liu, H. Zhao, et al., *ACS Appl. Mater. Interfaces* 13 (2021) 19904–19914.
- [48] X. Hu, J. Wang, J. Wang, et al., *Appl. Catal. B: Environ.* 318 (2022) 121879.
- [49] T. Zhao, D. Zhong, G. Hao, Q. Zhao, *Appl. Surf. Sci.* 607 (2023) 155079.
- [50] Ö. Şahin, D.E. Karakaş, M. Kaya, C. Saka, *J. Energy Inst.* 90 (2017) 466–475.
- [51] P. Li, Y. Huang, Q. Huang, et al., *Appl. Catal. B: Environ.* 313 (2022) 121444.
- [52] J. Li, X. Hong, Y. Wang, et al., *Energy Storage Mater.* 27 (2020) 187–197.
- [53] A. Tang, C. Wan, X. Hu, X. Ju, *Nano Res.* 14 (2021) 4063–4072.
- [54] Y. Huang, L. Zhang, L.W. Jiang, et al., *Small* 19 (2023) 2302970.
- [55] S. Zhou, L. Cheng, Y. Huang, et al., *Appl. Catal. B: Environ.* 328 (2023) 122519.
- [56] H. Li, Z. Liu, L. Wang, et al., *Chem. Eur. J.* 29 (2023) e202203207.
- [57] F.O. Baydaroglu, E. Özdemir, A.G. Gürek, *Int. J. Hydrog. Energy* 47 (2022) 9643–9652.
- [58] H. Zhang, L. Zhang, I.A. Rodríguez-Pérez, et al., *Appl. Surf. Sci.* 540 (2021) 148296.
- [59] P. Li, R. Chen, S. Zhao, et al., *Appl. Catal. B: Environ.* 298 (2021) 120523.
- [60] H. Zhang, Y. Liu, H. Wei, et al., *Appl. Catal. B: Environ.* 314 (2022) 121495.
- [61] S. Zhou, Y. Yang, W. Zhang, et al., *J. Colloid Interface Sci.* 591 (2021) 221–228.
- [62] H. Wu, Y. Cheng, B. Wang, et al., *J. Energy Chem.* 57 (2021) 198–205.
- [63] A. Sermiagin, D. Meyerstein, G.S. Rolly, et al., *Int. J. Hydrog. Energy* 47 (2022) 3972–3979.
- [64] U.B. Demirci, P. Miele, *C.R. Chim* 17 (2014) 707–716.